Multimodal Elucidation of Choline Metabolism in a Murine Glioma Model Using Magnetic Resonance Spectroscopy and ^{11}C-Choline Positron Emission Tomography

Hans F. Wehrl[1], Julian Schwab[1], Kathy Hasenbach[2,5], Gerald Reischl[1], Ghazaleh Tabatabai[2,5], Leticia Quintanilla-Martinez[3], Filip Jiru[6], Kamila Chughtai[7], Andras Kiss[7], Funda Cay[1], Daniel Bukala[1], Ron M.A. Heeren[7], Bernd J. Pichler[1], and Alexander W. Sauter[1,4,*]

Abstract

The metabolites, transporters, and enzymes involved in choline metabolism are regarded as biomarkers for disease progression in a variety of cancers, but their *in vivo* detection is not ideal. Both magnetic resonance spectroscopy [MRS using chemical shift imaging (CSI) total choline (tCho)] and ^{11}C-choline positron emission tomography (PET) can probe this pathway, but they have not been compared side by side. In this study, we used the spontaneous murine astrocytoma model SMA560 injected intracranially into syngeneic VM/Dk mice, analyzing animals at various postimplantation time points using dynamic microPET imaging and CSI MRS. We observed an increase in tumor volume and ^{11}C-choline uptake between days 5 and 18. Similarly, tCho levels decreased at days 5 to 18. We found a negative correlation between the tCho and PET results in the tumor and a positive correlation between the tCho tumor-to-brain ratio and choline uptake in the tumor. PCR results confirmed expected increases in expression levels for most of the transporters and enzymes. Using MRS quantification, a good agreement was found between CSI and ^{11}C-choline PET data, whereas a negative correlation occurred when CSI was not referenced. Thus, ^{11}C-choline PET and MRS methods seemed to be complementary in strengths. While advancing tumor proliferation caused an increasing ^{11}C-choline uptake, gliosis and inflammation potentially accounted for a high peritumoral tCho signal in CSI, as supported by histology and secondary ion mass spectrometry imaging. Our findings provide definitive evidence of the use of MRS, CSI, and PET for imaging tumors *in vivo*. *Cancer Res; 73(5); 1–11. ©2012 AACR.*

Introduction

Malignant gliomas are the most common primary brain tumors, which arise in approximately 18,000 people annually in the United States, thereby yielding high levels of morbidity and mortality (1). Even with optimal treatment, the median survival time following the diagnosis of a glioblastoma does not exceed 15 months (2). Current concepts about the origin and initiation of gliomas include a complex network of cellular and molecular interactions (3). Because of an enhanced cell proliferation and consecutive elevated levels of cell membrane synthesis during tumorigenesis as well as abnormal physiologic environments, such as hypoxia and acidic extracellular pH, choline metabolism is also involved in brain cancer (4). Choline is a precursor for the synthesis of the phospholipid components of the cell membrane. Cellular choline is phosphorylated by choline kinase (CK) yielding phosphocholine (PCho), which reacts further with CTP to yield CDP-choline. The *de novo* synthesis (Kennedy pathway) of phosphatidylcholine (PC) then results from the reaction of CDP-choline with diacylglycerol. Approximately, one half of the total membrane lipid content refers to PC (5). Several protein-mediated systems for choline transport exist: (i) high-affinity choline transporters (CHT), (ii) the choline transporter-like family (CTL), (iii) polyspecific organic cation transporters (OCT), and (iv) organic cation/carnitine transporters (OCTN). In the clinical setting, 2 imaging modalities allow for the examination of choline metabolism, namely proton magnetic resonance spectroscopy (^{1}H-MRS) and positron emission tomography (PET) using ^{11}C-choline. MRS provides noninvasive measurements of tissue concentrations of metabolites, such as total choline-containing compounds (tCho), total creatinine (tCr), and N-acetylaspartate (NAA). Increased tCho levels result from elevated

cell membrane turnover and cellular density (6). PCho and glycerophosphocholine (GPCho) are the major contributors of the tCho signal (7). While some authors recommend tCho/tCr ratios and compare them with the contralateral hemisphere (8), other groups favor tCho/tNAA ratios (choline to NAA index = CNI; ref. 9), which has a high correlation with the histologic grading (10). Doblas and colleagues have mentioned that both NAA and tCr levels can decrease during tumor progression, and therefore ratio variations could be relatively insensitive or even remain constant despite changes in the individual metabolite concentrations (11). ^{11}C-choline and its derivatives have been applied for neuro-oncologic PET imaging in the last years (12, 13). While the level of choline uptake in the normal brain is relatively low, the overexpression of the aforementioned amino acid transporters in tumors results in high tumor-to-background ratios. The modeling and quantification of the kinetic behavior of ^{11}C-choline is a challenging task, and a consentaneous approach has yet to be published. While Hara and colleagues have applied tumor-to-reference area radioactivity concentrations (14), Utriainen and colleagues have used the Patlak method (12). Interestingly, differences between the kinetic and the steady-state method were not observed (12).

Although MRS and ^{11}C-choline PET results reflect the choline metabolism, no statistical significance was found with either method (12). Because of this result, the conflicting data in the literature about reference tissues (e.g., the contralateral healthy brain) and metabolites (e.g., NAA) as well as the need for the validation and cross-correlation of both methods (15), we aimed to conduct a comparative *in vivo* study assessing tCho levels by MRS and ^{11}C-choline metabolism by PET with morphologic parameters in a murine orthotopic glioma mouse model. Such a cross-correlation of metabolic parameters *in vivo* is of special interest as an emerging imaging technology, hybrid PET/MRI, just entered the preclinical and clinical field (16, 17).

Materials and Methods

Cells and animal models

Murine SMA-560 (spontaneous murine astrocytoma) glioma cells (18) were cultured in Dulbecco's Modified Eagle's Medium containing 10% fetal calf serum, 2 mmol/L glutamine, and penicillin (100 IU/mL)/streptomycin (100 mg/mL). Five thousand SMA-560 cells were stereotactically implanted into the right hemisphere of 8- to 16-week-old male and female syngeneic VM/Dk mice on day 0. The local authorities approved the animal experiments. The PET and magnetic resonance measurements were conducted in 35 VM/Dk mice, some of these animals were studied longitudinally, which resulted in a total of 53 complimentary PET and magnetic resonance datasets. The measurements are grouped according to the postimplantation days (d) 5 to 18 (d5, $n = 4$; d6, $n = 4$; d7, $n = 4$; d8, $n = 10$; d11, $n = 4$; d12, $n = 8$; d14, $n = 11$; d16, $n = 6$; and d18, $n = 2$). Additional PCR data were obtained for 6 VM/Dk mice.

Imaging and spectroscopy

First, ^{11}C-choline was applied with a mean injected dose of 12.3 $\pm$ 1.2 MBq followed by dynamic microPET imaging (Inveon dedicated PET, Siemens Healthcare) with a spatial resolution in the reconstructed image of 1.4 mm. The following parameters were used: acquisition time 3,600 seconds, ordered subset expectation maximization reconstruction (16 subsets and 4 iterations), attenuation correction, and last 900 seconds summed frames for static image analysis. Subsequently, MRI was carried out in a 7 T small animal MRI scanner equipped with a 290 mT/m gradient system, a whole body quadrature coil for transmission, and a 4-channel mouse brain local coil for magnetic resonance signal reception (ClinScan, Bruker Biospin MRI). Chemical shift imaging spectroscopy data (3D PRESS-CSI; TR (repetition time) = 1,800 milliseconds; TE (echo time) = 135 milliseconds; matrix size, 16 $\times$ 16 $\times$ 16; voxel size = 1.3 mm $\times$ 1.3 mm $\times$ 1.3 mm; 2 averages; acquisition time 31 minutes 1 second) was acquired as follows: d5, $n = 2$; d6, $n = 2$; d7, $n = 2$; d8, $n = 4$; d11, $n = 4$; d12, $n = 5$; d14, $n = 6$; d16, $n = 4$; and d18, $n = 1$. Automatic and manual shimming was conducted for an adjustment volume of 6 mm $\times$ 3 mm $\times$ 5 mm centered in the brain.

Image analysis

Inveon research workplace (IRW, Version 3.0, Siemens Healthcare) was used for image fusion and data analysis. After PET and magnetic resonance image fusion, the regions of interest (ROI) for brain tumor (tumor), normal contralateral brain (brain), and cerebellum were defined on the basis of the T2-weighted magnetic resonance images. Care was taken to exclude the hyperintense regions for the nontumor regions. As the magnetic resonance sequences covered only the animal brain, the muscle ROIs were identified on the foreleg musculature using the PET datasets. CSI data processing was conducted using an automatic postprocessing routine jSIPRO (java Spectroscopic Imaging PROcessing, Version 0.9, https://www.sites.google.com/site/jsiprotool) based on LCModel (Version 6.2; ref. 19). Spectroscopic images in DICOM format were generated by jSIPRO and imported into IRW for further evaluation. Choline-containing compounds (tCho, at 3.2 ppm) and NAA (at 2.0 ppm) values were obtained from the anatomic ROIs placed on the corresponding CSI maps. Subsequently, the PET data were evaluated using the same ROIs as was applied for magnetic resonance data analysis (except muscle ROIs). The PET data were normalized to the respective amount of injected radioactivity, which is reported as %ID/mL (percentage injected dose per milliliter). Furthermore, PET, CSI, and magnetic resonance data were referenced to different reference regions, thereby yielding the following ratios: tumor-to-brain ratio, tumor-to-cerebellum ratio, and tumor-to-muscle ratio. Details about the correlation analysis between PET and CSI data in 5 example datasets can be found in the Supplementary Material and Methods.

mRNA expression

PCR data were obtained from 3 animals each, sacrificed on days 11 and 15 postimplantation. The detailed PCR methods can be found in the Supplementary Material and Methods.

Histology

After sacrificing the animals, the mouse brain tissue was dissected from the cranial cavity and fixed in zinc salt solution for 24 hours (20). The tissue was subsequently dehydrated with an increasing gradient of alcohol and embedded in paraffin. The tissue specimens were cut into 5-μm sections and stained with hematoxylin and eosin (H&E). Immunohistochemistry was carried out using an automated immunostainer (Ventana Medical Systems, Inc.) according to the company's protocols for open procedures with slight modifications. The antibody panel used included Ki-67 (SP6; Thermo Fisher Scientific), CD31 (ab28364; Abcam), cleaved caspase-3 (ASP 175; Cell Signaling Technology), CD3 (SP7; DCS Innovative Diagnostik-Systeme GmbH & Co. KG), and glial fibrillary acidic protein (GFAP; 6F2; Dako Deutschland GmbH). The appropriate positive controls were used to confirm adequate staining. The histologic samples were analyzed by an experienced pathologist (L. Quintanilla-Martinez).

Secondary ion mass spectrometry—mass spectrometry imaging

For the visualization of the distribution of choline metabolites, our histologic methods were complemented by secondary ion mass spectrometry—mass spectrometry imaging (SIMS-MSI). For details of the methodology please refer to the Supplementary Materials and Methods.

Statistical analysis

Descriptive statistics including, the mean and 1 SD values, were calculated with SigmaPlot 11.0 (Systat Software, Inc.). Correlation analysis between CSI and PET values was based on ROIs defined by anatomic magnetic resonance and placed to the respective CSI and PET datasets. The correlation between the pairs of variables was evaluated using the Pearson product-moment coefficient. Statistical significance was considered with $P \leq 0.05$.

Results

Magnetic resonance-volumetry

The mean volumes of the intracranial tumors derived from the T2-weighted images increased exponentially between day 5 (6.93 ± 3.49 mm^3) and 18 (107.20 ± 29.13 mm^3; Fig. 1A). Interestingly, the strongest increase is noticeable starting from day 11, in which the tumor volume quintupled from 12.25 ± 5.02 to 61.62 ± 29.53 mm^3 on day 14.

^{11}C-choline PET

This trend was also observed with the analysis of ^{11}C-choline uptake in the tumor, which starts to prominently increase from 1.27 ± 0.55%ID/mL on day 12 to 3.93 ± 0.28%ID/mL on day 18 (Fig. 1B). This increase is highly significant ($P < 0.001$). A first peak in ^{11}C-choline uptake at day 7 and a subsequent decrease until day 12 was observed. Finally, the injected doses increased until day 18. The PET tumor-to-brain and tumor-to-cerebellum ratios are presented in the Fig. 1C and D. More detailed values can be found in the Supplementary Results.

Chemical shift imaging

The mean tumor tCho values (in arbitrary units, a.u.) decreased from day 5 ($5.35 \pm 1.65 \times 10^4$ a.u.) until day 7 ($2.42 \pm 0.11 \times 10^4$ a.u.). From day 8 ($2.99 \pm 1.26 \times 10^4$ a.u.) until day 16 ($2.94 \pm 1.44 \times 10^4$ a.u.) a plateau was observed. Day 18 indicates a further decrease (1.78×10^4 a.u.) in tCho levels (Fig. 1E). Tumor-to-brain ratios ranged from 1.20 ± 0.09 on day 5 to 2.08 on day 18 (Fig. 1F), whereas the tumor-to-cerebellum ratios for choline-CSI did not continuously increase with a minimum value at day 6 (0.57 ± 0.22) and a maximum value at day 11 (4.45 ± 2.49). The tumor NAA values decreased from day 5 ($15.20 \pm 5.13 \times 10^4$ a.u.) to day 18 (0.36×10^4 a.u.). The metabolite values (averaged from day 5 until day 18) observed in the brain were $2.72 \pm 1.33 \times 10^4$ a.u. for tCho and $7.30 \pm 4.11 \times 10^4$ a.u. for NAA (decreasing from $137.00 \pm 38.50 \times 10^4$ a.u. (d5) to $4.09 \pm 2.52 \times 10^4$ a.u. (d12) and decreased further to 1.62×10^4 a.u. on day 18), whereas the values for the cerebellum were $2.86 \pm 2.54 \times 10^4$ a.u. for tCho and $3.56 \pm 3.05 \times 10^4$ a.u. for NAA. Figure 2 shows an example of PET (Fig. 2A), T2-weighed magnetic resonance imaging (Fig. 2B), CSI data (Fig. 2C) with tumor (Fig. 2D), and brain spectra (Fig. 2E) of a mouse brain with glioma on postimplantation day 18.

Correlations between ^{11}C-choline PET and chemical shift imaging

The Supplementary Table 1S in the Supplementary Results summarizes the correlations between the values and ratios derived from PET and CSI analyses from day 5 to 18. Identical ROIs for each animal, based on the anatomic magnetic resonance-volumetry images, were used for the respective CSI and PET correlation analysis. Negative correlations were observed between tCho and ^{11}C-choline PET tumor-to-brain ratio ($r = -0.680$; $P = 0.044$), tCho and ^{11}C-choline PET tumor-to-cerebellum ratio ($r = -0.812$; $P = 0.008$). Positive correlations were observed between tCho tumor-to-brain ratio and %ID/mL in the tumor ($r = 0.839$; $P = 0.005$), tCho tumor-to-brain ratio, and ^{11}C-choline PET tumor-to-brain ratio ($r = 0.693$; $P = 0.038$) as well as tCho tumor-to-brain ratio and ^{11}C-choline PET tumor-to-cerebellum-ratio ($r = 0.659$; $P = 0.054$). The other comparisons revealed no significant correlations. In addition, no correlations were observed between tCho and %ID/mL, NAA and %ID/mL, tCho/NAA and %ID/mL in the normal brain and cerebellum, respectively.

Typical examples (postimplantation days 12–14) of ^{11}C-choline PET, CSI, and T2-weighted–based tumor ROIs of the maximal values are presented in Fig. 3. A visual and a quantitative voxel-wise correlation of PET and CSI values in the tumor ROI reveal overall a low correlation between these 2 measurements (Fig. 3A–E). There is only a small overlap between tumor volumes as identified by CSI and PET (Fig. 3F and I). Highest PET uptake values are present in the intersection between tumor volume as defined by anatomic magnetic resonance imaging and PET (Fig. 3G). The CSI defined tumor volume reveals only a low PET uptake (Fig. 3G), but CSI choline tumor/brain ratios are largest in this volume as well as its intersection with anatomic or PET based information (Fig. 3H). The Venn diagram summarizes these findings of complementarity between PET and CSI tumor volume information (Fig. 3I).

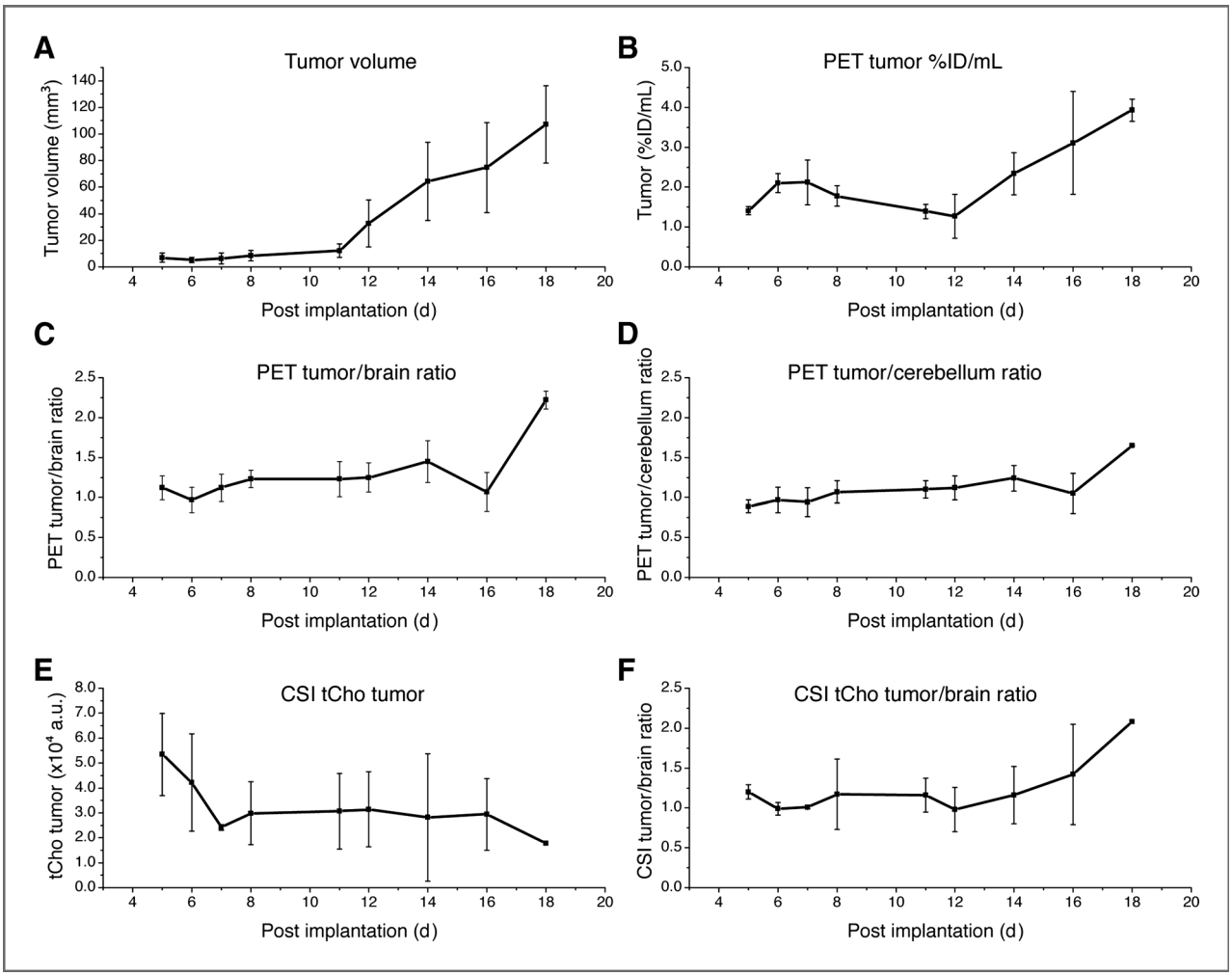

Figure 1. Image-derived parameters of tumor growth and choline metabolism as a function of postimplantation time. A, tumor volume increased steadily and quintupled from day 11 to 18. B, tumor ^{11}C-choline uptake (provided as %ID/mL) displayed an initial maximum value at day 7, which decreased until day 12 and then further increased until day 18. C and D, tumor-to-brain ratios of choline uptake (C) and tumor-to-cerebellum ratios (D) displayed a similar pattern with a slight ratio drop at day 16. E, CSI tCho levels displayed a plateau from day 8 to 16 and then decreased. F, using a reference tissue, such as the contralateral brain, switched the decrease into an increase.

mRNA expression

The mRNA expression levels of CHT1, CTL1-4, OCT1-2, CK-α, CK-β, and PHLD for days 11 and 15 in the tumor, brain, and cerebellum tissues are summarized in Fig. 4. Referenced to the brain tissue, most of these important transporters and enzymes were upregulated but displayed a decrease in expression between day 11 and 15. Additional details can be found in the Supplementary Results.

Histology

On the basis of the histologic analysis, the tumors were composed of relatively large cells with hyperchromatic and polymorphic nuclei typically with one or more prominent nucleoli (Fig. 5A and E). All tumors displayed a relatively high mitotic rate and areas of necrosis primarily in the center of the tumors at the later postimplantation days. The levels of proliferation as shown with the Ki-67 antibody (Fig. 5B, F, and I) increased relative to the size of the tumor and days after implantation as well as the amount of vascularization visualized by CD31 staining (Fig. 5J). Although apoptosis increased with the size of the tumors, cell death was primarily observed in the center of the lesion, as shown by assessing the levels of activated caspase-3 expression (Fig. 5K). The stains for GFAP showed a strong specific reaction in glial cells predominantly around the tumors, indicating reactive gliosis against the tumor cells (Fig. 5C and G). The formation of gliosis is increasing from day 14 to 18. The CD3 staining shows a substantial infiltration of T cells on day 18 but not for day 14 (Fig. 5D, H, and L).

Secondary ion mass spectrometry—mass spectrometry imaging

Figure 6 presents the distributions of free choline (m/z 104) and PCho (m/z 184) in a mouse control brain and a tumor-bearing brain at day 15.

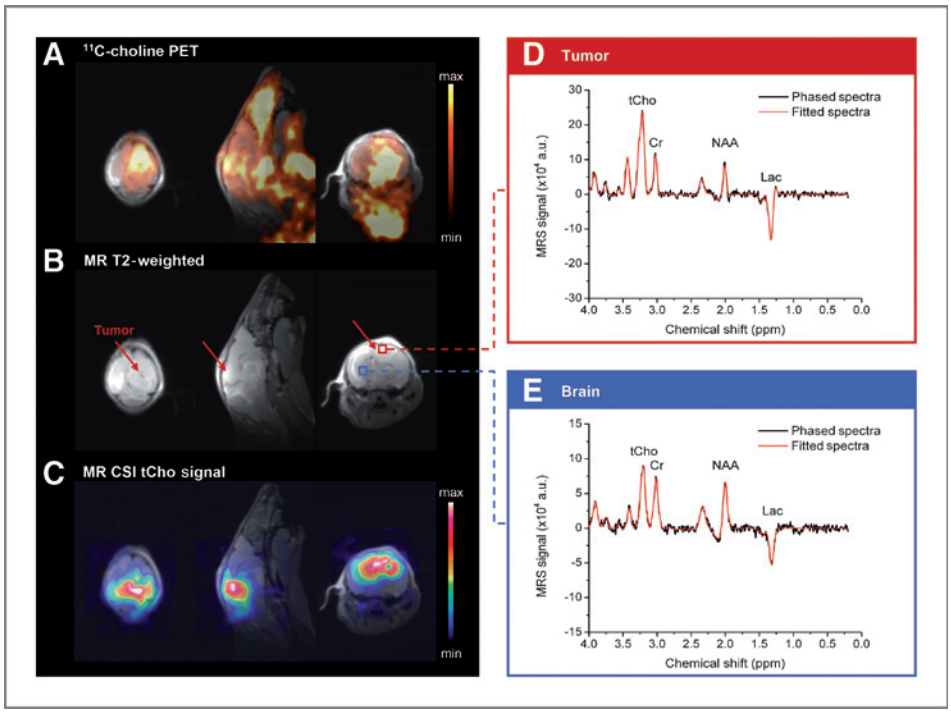

Figure 2. ^{11}C-choline PET (A), T2-weighted magnetic resonance sequence (B), CSI map (C), tumor (D), and brain (E) spectra of a murine glioma at postimplantation day 18.

Discussion

To date, it is not fully understood whether ^{1}H-MRS and ^{11}C-choline PET reflect the same or different parts of the choline pathway and whether the imaging parameters are complementary or not. Therefore, we have conducted a small animal imaging study on a syngeneic glioma model using VM/Dk mice with orthotopically implanted SMA-560 cells and subsequently validated the *in vivo* results with *in vitro* and *ex vivo* techniques. In such a syngeneic tumor model, immunodeficiency is not required as is with xenograft models; therefore, the tumor growth and microenvironmental characteristics resemble more closely the clinical conditions.

The levels of choline uptake increased over time, which is reflected by a range of the tumor-to-brain ratio values from 1.12 ± 0.15 for day 5 to 2.22 ± 0.11 for day 18. These results are comparable with the human data reported by Kato and colleagues, which displays a tumor-to-brain ratio of 2.69 ± 2.04 in grade 2 astrocytic tumors. However, both grade 3 and 4 tumors have a higher tumor-to-brain ratio with 4.76 ± 3.04 (grade 3) and 18.35 ± 6.73 (grade 4; ref. 21). Our standardized uptake values (SUV) values ranged from 0.31 to 0.71, which are lower as compared with a C6 glioma rat model (2.00 ± 0.53; ref. 13). The lower values are due to the chemically modified tracer, the different tumor entities, the partial volume effects, and the different weight composition of rats compared with mice. The shape of the tumor %ID/mL curve reveals the first maximum at day 7, which decreased until day 12 and then increased again until day 18 (Fig. 1B). We hypothesize that the shape of the curve is caused by a complex interplay of transporter regulation and partial volume effects. At the initiation of tumor growth, a majority of the transporters are upregulated (see the PCR data for day 11 and Supplementary Discussion), thereby causing an increase in choline uptake. This measured choline uptake in tumors is amplified by a strong partial volume effect in the small tumors during the initial phase. The rapid tumor growth following the initial phase reduces the partial volume effect in combination with a transporter downregulation, which is reflected in a reduction in the %ID/mL values until day 12. As the tumors further progress, the %ID/mL values increased in proportion with the tumor volume. Both the tumor-to-brain and tumor-to-cerebellum ratio curves reflect this trend but exhibit another minimum on day 16 (Fig. 1C and D). The tumor-to-muscle ratio values became increasingly unsteady over time, which is a phenomenon that might be caused by altered muscle metabolism due to cachexia.

The acquired CSI data reflecting the tCho levels in the tumors ranged from 5.35×10^4 a.u. for day 5 to 1.78×10^4 a.u. for day 18. As the CSI acquisitions do not allow for an absolute quantification without further processing, it is difficult to compare our results with other data in the literature. However, the shape of the CSI spectra is qualitatively comparable with those acquired in a clinical setting (Fig. 2D). In the human brain, the choline-containing compounds were found at a concentration of 64.3 ± 10.1 μmol/100 g (human brain), whereas astrocytomas and anaplastic astrocytomas display concentrations of choline-containing compounds of 68.6 ± 6.5 μmol/100 g and 132.6 ± 7.9 μmol/100 g, respectively (22). On the basis of the tumor-to-brain ratios, the values are 1.07 for astrocytoma and 2.06 for anaplastic astrocytoma. These values correspond with our glioma model, in which the tumor-to-brain ratios range from 1.20 for day 5 to 2.08 for day

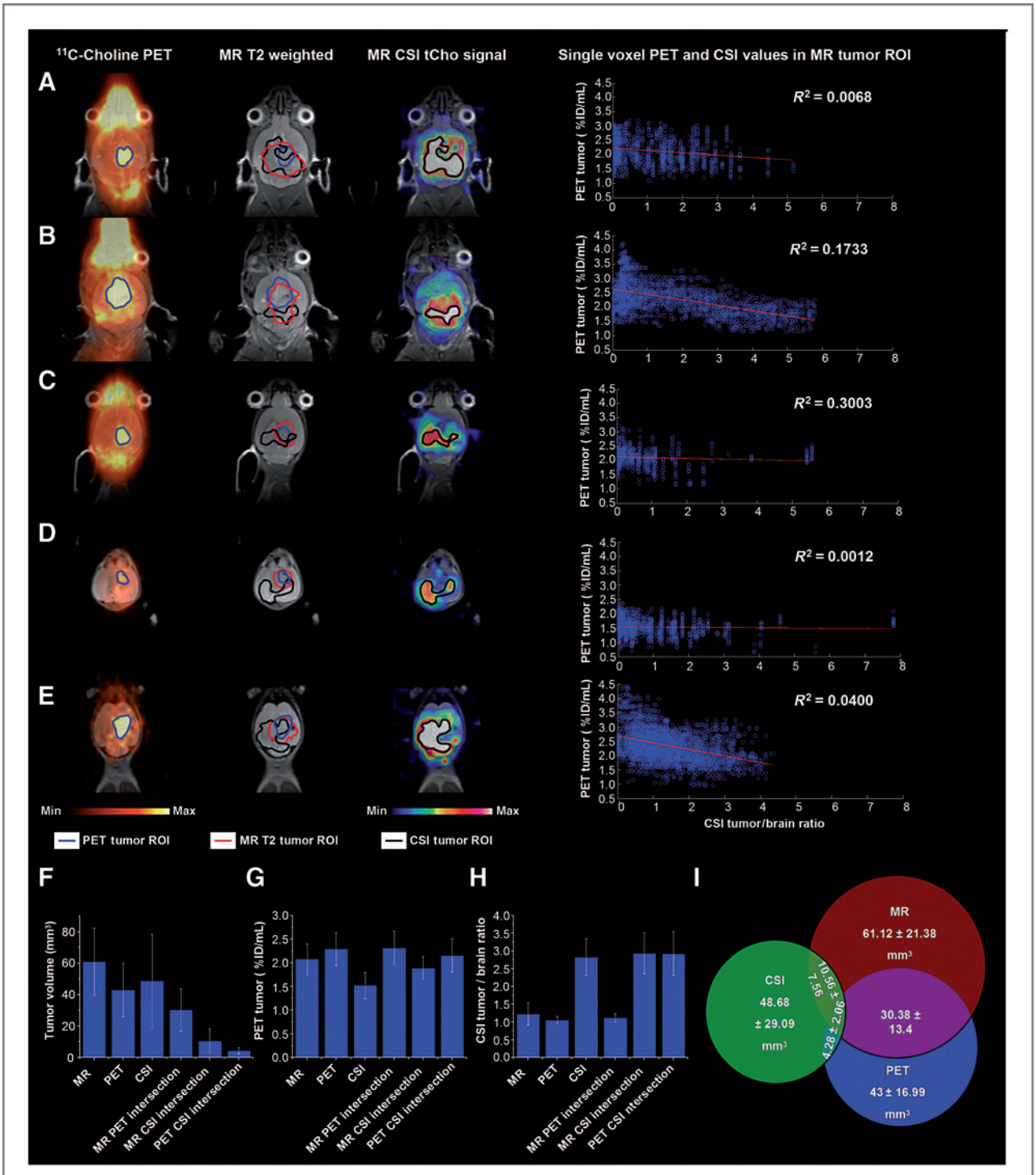

Figure 3. Complementarities between ^{11}C-choline PET and CSI tumor ROIs in 5 different examples (postimplantation days 12–14). Tumor ROIs based on ^{11}C-choline PET (first column), T2-weighted magnetic resonance anatomy (second column), and magnetic resonance CSI tCho signal (third column) and the voxel-wise correlation of the PET and CSI values in the anatomy magnetic resonance–based tumor ROI (fourth column) are presented. The PET-based tumor ROIs are usually smaller and localized toward the center of the tumor, whereas the CSI ROI covered primarily the tumor rim and spread into the surrounding brain areas. The corresponding voxel-wise PET and CSI data show a low correlation (A–E). Quantitative analysis of the volumes based on the different modalities and its intersections (F), PET tumor uptake (G) as well as CSI values (H) reveal the complementary nature in these examples.The Venn diagram (I) visualizes the tumor volumes with intersections.

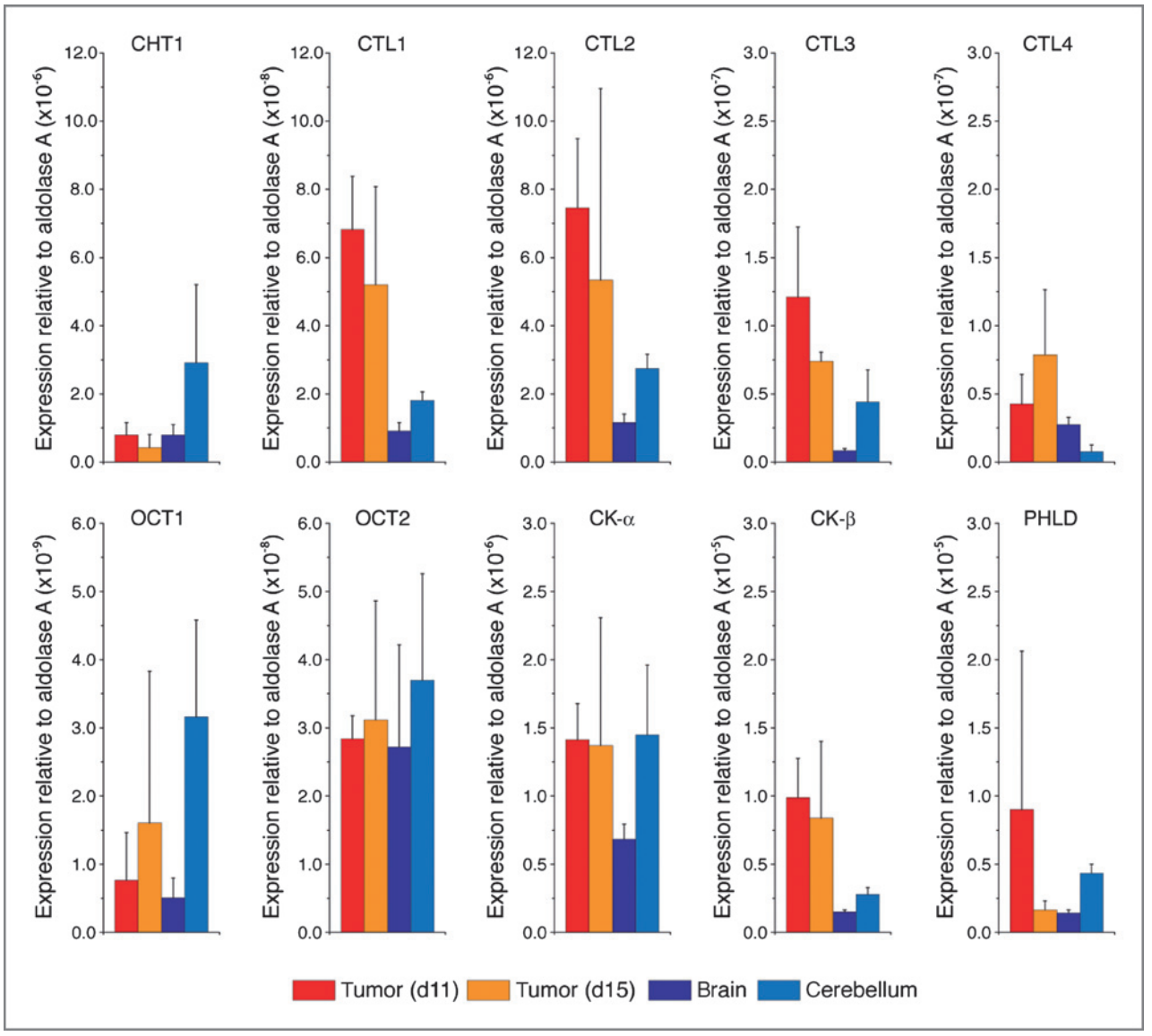

Figure 4. RNA expression levels of CHT1, CTL1-4, OCT1-2, CK-α, CK-β, and PHLD in the tumor at days 11 and 15; the brain and cerebellum were referenced to aldolase A.

18. Interestingly, Usenius and colleagues have displayed a decrease in the absolute concentrations of choline in astrocytoma grade 4 (1.62 ± 0.28 mmol/L) compared with the control (1.74 ± 0.09 mmol/L), astrocytoma grade 1–2 (1.93 ± 0.09 mmol/L) and astrocytoma grade 3 (1.95 mmol/L), whereas the PC/(PC + GPC) ratio increased (23). This decrease toward the later tumor stages is also reflected by our data. However, also a decrease in the contralateral hemisphere is present resulting in an increase of the tumor-to-brain ratios. Possible explanations for this phenomenon could be different choline concentrations in the brain (24), accelerated aging (25, 26) and glioma-induced neurodegenerative processes (27), reduced global cerebral blood flow (28), and ischemia (29). Doblas and colleagues have also observed significant variations and heterogeneity in different rodent gliomas, such as the F98 model (8.1 ± 12.4; ref. 11). Therefore, we conclude that our MRS and PET data are in accordance with the corresponding human and small animal data in the literature. The increase of tumor volume from day 5 through 18 was paralleled by increased contrast enhancement (days 8–16) as well as progression of proliferation and vascular density confirmed by histology.

In this study, we observed negative correlations between the tCho and ^{11}C-choline PET tumor-to-brain ratio ($r = -0.680$; $P = 0.044$) and the tCho and ^{11}C-choline PET tumor-to-cerebellum ratio ($r = -0.812$; $P = 0.008$). Because of the decreasing tCho levels in the brain as a reference tissue (see Supplementary Discussion), positive correlations were observed between the tCho tumor-to-brain ratio and %ID/mL ($r = 0.839$; $P = 0.005$), the tCho tumor-to-brain ratio and the ^{11}C-choline PET tumor-to-brain ratio ($r = 0.693$; $P = 0.038$).

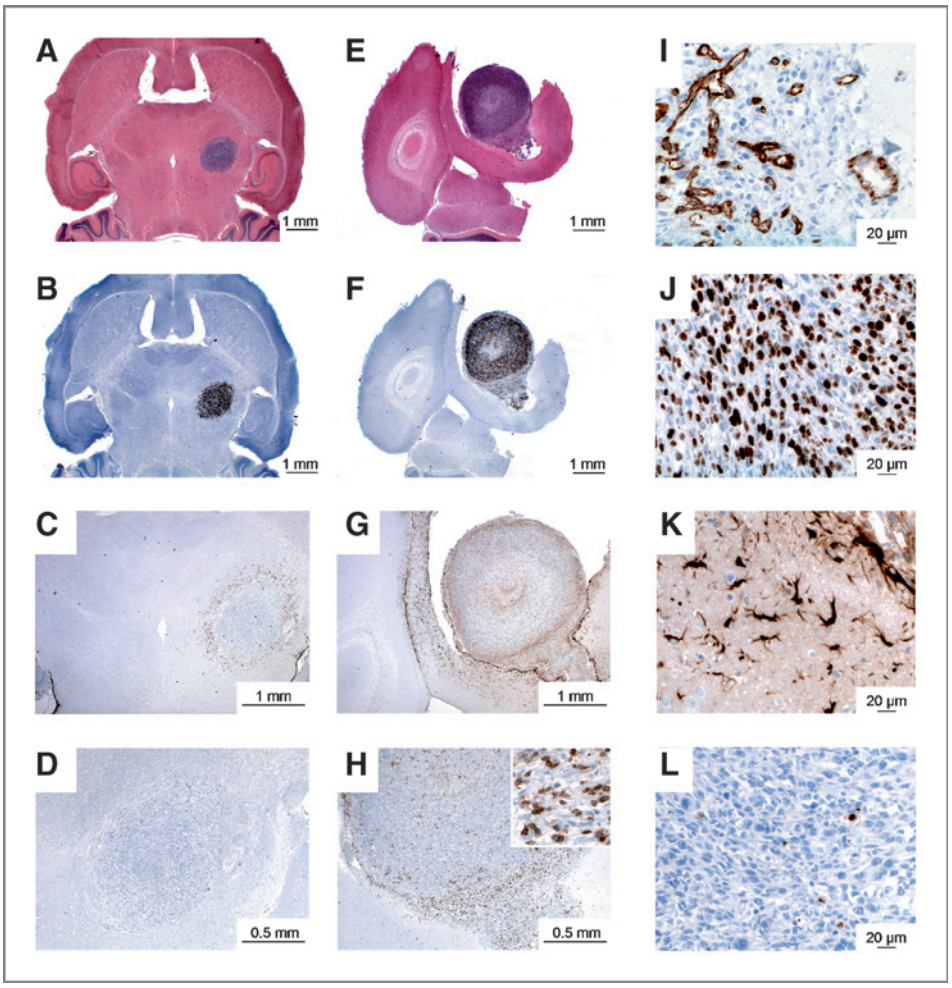

Figure 5. Histologic analysis of a murine glioma at postimplantation day 14 (A and B, magnification ×12.5; C, magnification ×25; D, magnification ×50) and day 18 (E and F, magnification ×12.5; G, magnification ×25; H, magnification ×50; I–L, magnification ×400). A and B, H&E (A) and Ki-67 (B) staining show a small, highly proliferative tumor localized in the thalamic region. E, H&E staining revealing the tumor with dense, polymorphic nuclei, central necrosis, and infiltration of the ventricular system. In addition, a high proliferation rate as presented by Ki-67 staining (F and J) and vascularity as reflected by CD31 assessment (I) were observed. Some apoptotic areas were seen in the center of the lesion as displayed with caspase-3 staining (L). The stains for GFAP showed a strong specific reaction in glial cells predominantly around the tumors, indicating reactive gliosis against the tumor cells, whereas the tumor cells were GFAP-negative (C, G, and K). The lack of GFAP reactivity in the tumor cells could be interpreted as lack of differentiation of the tumor cells. The formation of gliosis increased from day 14 (C) to day 18 (G and K). The CD3 staining shows no reactive T lymphocytes on day 14 (D), but a substantial infiltration on day 18 (H).

These correlations were obtained when including all the data in the analysis. Because of the significant aggressiveness of the tumor, the group sizes at the last postimplantation days were small. The exclusion of the day 18 data from the analysis impaired the statistical significance of the correlations as follows: the tCho and ^{11}C-choline PET tumor-to-cerebellum ratio ($r = -0.754$; $P = 0.031$), the tCho and ^{11}C-choline PET tumor-to-brain ratio ($r = -0.537$; $P = 0.170$), and the tCho tumor-to-brain ratio and %ID/mL ($r = -0.555$; $P = 0.153$). In opposition to our findings, Utriainen and colleagues have failed to observe a significant correlation between the tCho levels determined by ^{1}H-MRS and ^{11}C-choline uptake ($r = 0.50$–0.54; $P = 0.1$; ref. 12). They have declared that it is uncertain whether the association should be expected because the choline-containing component of MRS represents intracellular metabolite pools of PCho and GPCho, whereas the rate of choline uptake is thought to be controlled by amino acid transporter expression and attenuation in tumor endothelial cells (12). However, in this study, only 8 patients had malignant brain tumors and there was a time lag of a few days between the 2 imaging studies. Both the small sample size and the rapid tumor proliferation might have changed within a few days, which may explain their findings. Rommel and colleagues have observed a correlation between choline levels and ^{18}F-FCH uptake ranging from 0.12 to 0.33 with P values ranging from 0.054 to 0.48 (30). They concluded that high choline levels correlated with low values for ^{18}F-FCH uptake and vice versa.

Kato and colleagues have displayed a positive correlation between ^{11}C-choline tracer uptake and the proliferation index in astrocytic tumors ($r = 0.64$; $P < 0.001$; ref. 21), which is supported by our data. Shimizu and colleagues have reported a strong linear relationship between the Ki-67–labeling index and the MRS tCho levels ($r = 0.81$; $P < 0.0001$) and a weak correlation between the tCho/NAA ratio ($r = 0.60$; $P < 0.02$; ref. 31). Our data suggest a negative correlation between tCho levels and the proliferation index; although, when tCho levels were referenced to either the brain or cerebellum, we observed a positive correlation (see Supplementary Discussion).

We also observe complementary data with ^{11}C-choline PET and CSI results in the qualitative outline of the tumor presented as maximal values. CSI highlights the areas of high choline concentration, which seems to be localized to the tumor rim, whereas ^{11}C-choline PET identifies the regions of high choline turnover. Tumor spread to normal brain tissue seems to be better characterized by CSI, which indicates also

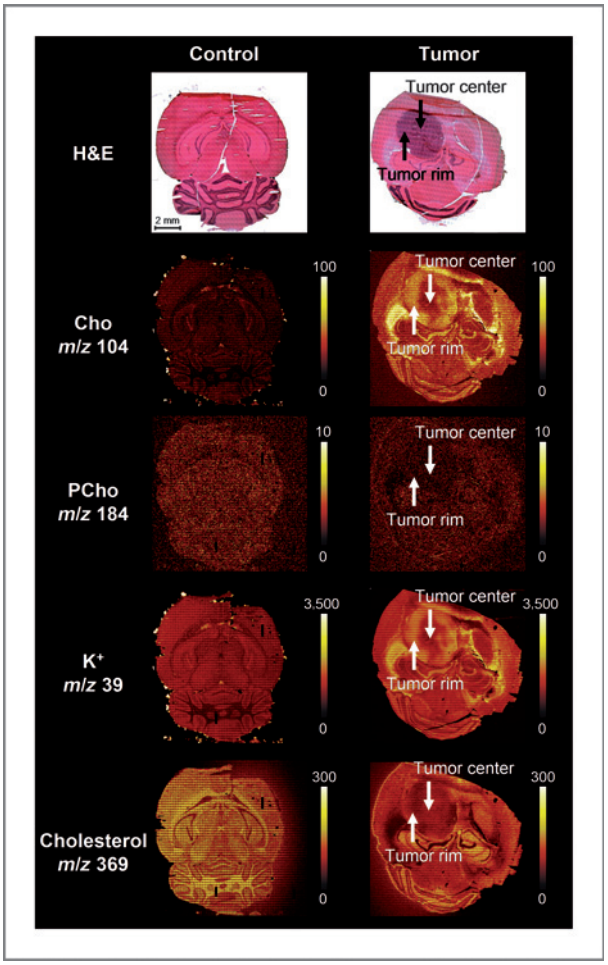

Figure 6. SIMS imaging in a control and glioma-bearing mouse brain. Top, images of H&E-stained sections of control and tumor-bearing mouse brains. Bottom, SIMS distributions of the choline ion (*m/z* 104), phosphocholine molecular ion (*m/z* 184), potassium (K^+; *m/z* 39), and dehydrated cholesterol ion ($[M\text{-}H_2O+H]^+$; *m/z* 369) in the mouse control brain as well as brain with implanted tumor. The increased signal of choline and potassium ions was detected from the rim of the tumor. The intensity of potassium detected from the ventricles was higher in tumor-bearing brain section as compared with the control brain section. Lower PCho intensity was detected from the tumor region compared with the normal brain tissue. Cholesterol molecular ion was detected from brain regions presenting low potassium ion intensity. H&E-staining and metabolite values indicate a necrosis in the tumor center, however, the tumor rim consists of proliferative cells. The semilunar-shaped region adjacent the tumor with elevated choline and K^+ signals refers to the choroid plexus, where cerebrospinal fluid is produced. Color bars indicate absolute ion counts.

high tCho levels in the vicinity of the tumor, not observed in ^{11}C-choline PET in these areas. Rand and colleagues documented white blood cell infiltrates in most of the false positive lesions analyzed with MRS (32). The authors hypothesized that these infiltrates are a source of elevated choline. In addition, Srinivasan and colleagues found that gliosis in response to surgical trauma and therapeutic modalities may be indistinguishable from tumor growth (33). Using GFAP and CD3 immunohistochemistry, we could disclose that gliosis and inflammation are increasingly found in the later tumor stage of our murine model. Therefore, the CSI tCho signal at the tumor periphery is potentially linked to inflammation and gliosis, whereas the ^{11}C-choline PET uptake in the tumor core is linked to proliferative tumor cells. These results are in the line with metabolic imaging derived from SIMS-MSI. Here, the free choline is predominantly located in the tumor rim, whereas PCho can be found in the tumor periphery yielding a high tCho CSI signal. On the other hand, the specific ^{11}C-choline PET tracer accumulates more in the proliferative tumor parts.

Our study has several limitations. Because of the significant aggressiveness and the rapid growth rates of the tumors, the animals were susceptible to prolonged imaging times. Because of the animal protection and ethical concerns, animals had to be sacrificed as soon as they exhibited impairments caused by the tumor. This resulted in heterogeneous group sizes. The high morbidity of the animals did not allow for an acquisition of the full image parameters for PET and magnetic resonance. PET and magnetic resonance measurements were conducted sequentially; therefore, small offsets in coregistration must be expected. However, as the brain is stabilized by the skull, coregistration errors between PET and magnetic resonance measurements are on the order of less than 1 mm. As both the PET and CSI voxel sizes are above this limit, we concluded that these errors are negligible. We were unable to conduct an absolute quantification of the choline CSI data because the inclusion of a reference sample would have prevented the use of a tight fitting local coil on the brain of the animal, which would have influenced the signal-to-noise ratio and magnetic resonance image quality. Furthermore, an additional magnetic resonance CSI scan without water suppression was not conducted because this would have significantly extended the measurement time per animal. Given the increased rate of morbidity of the animals at later stages of tumor growth, we aimed to both reduce the time during which the animals were under anesthesia as much as possible and conduct imaging protocols that are feasible in a clinical setting, which are also streamlined for patient comfort and throughput.

In this study, we monitored tumor progression in a mouse glioma model. We found that the magnetic resonance CSI data of choline metabolism were in agreement with the PET ^{11}C-choline data when a reference region, such as the normal brain, was used for MRS quantification. It is important to take into account that the detection limit for MRS techniques is in the 10^{-3} to 10^{-6} mol/L range, whereas the PET method concentration limit is 10^{-12} mol/L. Furthermore, we found that the ^{11}C-choline PET data of brain tumors correlated with both PCR and histologic analyses. Absolute quantification of ^{11}C-choline PET data was more reliable compared with the MRS technique. Therefore, we suggest that these methods have complimentary roles, with MRS functioning as a tool for qualitative tumor assessment, early indication of tumor spread, gliosis and inflammation, whereas ^{11}C-choline PET serves as an imaging biomarker for proliferation, and is therefore of interest for treatment planning and therapy monitoring.

Disclosure of Potential Conflicts of Interest

Bernd Pichler received grant/research support from Siemens, AstraZeneca, Bayer Healthcare, Boehringer-Ingelheim, Oncodesign, Merck, Bruker, and the Werner Siemens-Foundation. No potential conflicts of interest were disclosed by the other authors.

Authors' Contributions

Development of methodology: H.F. Wehrl, A.W. Sauter, F. Jiru, R.M.A. Heeren, B.J. Pichler

Acquisition of data (provided animals, acquired and managed patients, provided facilities, etc.): H.F. Wehrl, A.W. Sauter, G. Reischl, K. Hasenbach, F. Cay, D. Bukala, L. Quintanilla-Martinez, G. Tabatabai, A. Kiss

Analysis and interpretation of data (e.g., statistical analysis, biostatistics, computational analysis): H.F. Wehrl, J. Schwab, A.W. Sauter, K. Chughtai, A. Kiss

Writing, review, and/or revision of the manuscript: H.F. Wehrl, J. Schwab, K. Hasenbach, G. Reischl, G. Tabatabai, L. Quintanilla-Martinez, F. Jiru, K. Chughtai, A. Kiss, F. Cay, D. Bukala, R.M.A. Heeren, B.J. Pichler, A.W. Sauter

Study supervision: H.F. Wehrl, A.W. Sauter

Acknowledgments

The authors thank Maren Koenig and Mareike Lehnhoff for the excellent technical support and Ursula Kohlhofer for help with the histology during this project. We also appreciate the development and support of the jSIPRO tool by Antonin Skoch and Milan Hajek from the Institute for Clinical and Experimental Medicine.

Grant Support

This study was supported by German Research Foundation (DFG PI 771/1-1, SFB 773), the Werner Siemens-Foundation, and Ministry of Health Czech Republic [grant: 00023001 Institute for Clinical and Experimental Medicine (IKEM), Prague]. SIMS work is part of the research program of the "Foundation for Fundamental Research on Matter (FOM)," financially supported by the "the Netherlands Organization for Scientific Research (NWO)."

The costs of publication of this article were defrayed in part by the payment of page charges. This article must therefore be hereby marked *advertisement* in accordance with 18 U.S.C. Section 1734 solely to indicate this fact.

Received June 28, 2012; revised October 31, 2012; accepted November 23, 2012; published OnlineFirst January 23, 2013.

References

1. (CBTRUS) CBTRotUS. CBTRUS statistical report: primary brain and central nervous system tumors diagnosed in the United States in 2004–2006 Central Brain Tumor Registry of the United States, Hinsdale, IL; 2010.
2. Stupp R, Hegi ME, Mason WP, van den Bent MJ, Taphoorn MJ, Janzer RC, et al. Effects of radiotherapy with concomitant and adjuvant temozolomide versus radiotherapy alone on survival in glioblastoma in a randomised phase III study: 5-year analysis of the EORTC-NCIC trial. Lancet Oncol 2009;10:459–66.
3. Mazzoleni S, Galli R. Gliomagenesis: a game played by few players or a team effort? Front Biosci (Elite Ed) 2012;4:205–13.
4. Glunde K, Bhujwalla ZM, Ronen SM. Choline metabolism in malignant transformation. Nat Rev Cancer 2011;11:835–48.
5. Michel V, Yuan Z, Ramsubir S, Bakovic M. Choline transport for phospholipid synthesis. Exp Biol Med (Maywood) 2006;231:490–504.
6. Law M, Yang S, Wang H, Babb JS, Johnson G, Cha S, et al. Glioma grading: sensitivity, specificity, and predictive values of perfusion MR imaging and proton MR spectroscopic imaging compared with conventional MR imaging. AJNR Am J Neuroradiol 2003;24:1989–98.
7. Boulanger Y, Labelle M, Khiat A. Role of phospholipase A(2) on the variations of the choline signal intensity observed by 1H magnetic resonance spectroscopy in brain diseases. Brain Res Brain Res Rev 2000;33:380–9.
8. Imani F, Boada FE, Lieberman FS, Davis DK, Deeb EL, Mountz JM. Comparison of proton magnetic resonance spectroscopy with fluorine-18 2-fluoro-deoxyglucose positron emission tomography for assessment of brain tumor progression. J Neuroimaging 2012;22:184–90.
9. Saraswathy S, Crawford FW, Lamborn KR, Pirzkall A, Chang S, Cha S, et al. Evaluation of MR markers that predict survival in patients with newly diagnosed GBM prior to adjuvant therapy. J Neurooncol 2009;91:69–81.
10. Frati A, Pichierri A, Bastianello S, Raco A, Santoro A, Esposito V, et al. Frameless stereotactic cerebral biopsy: our experience in 296 cases. Stereotact Funct Neurosurg 2011;89:234–45.
11. Doblas S, He T, Saunders D, Hoyle J, Smith N, Pye Q, et al. *In vivo* characterization of several rodent glioma models by (1) H MRS. NMR Biomed 2012;25:685–94.
12. Utriainen M, Komu M, Vuorinen V, Lehikoinen P, Sonninen P, Kurki T, et al. Evaluation of brain tumor metabolism with [11C]choline PET and ^{1}H-MRS. J Neurooncol 2003;62:329–38.
13. Wyss MT, Spaeth N, Biollaz G, Pahnke J, Alessi P, Trachsel E, et al. Uptake of 18F-fluorocholine, 18F-FET, and 18F-FDG in C6 gliomas and correlation with 131I-SIP(L19), a marker of angiogenesis. J Nucl Med 2007;48:608–14.
14. Hara T, Kosaka N, Shinoura N, Kondo T. PET imaging of brain tumor with [methyl-11C]choline. J Nucl Med 1997;38:842–7.
15. Gulyas B, Nyary I, Borbely K. FDG, MET or CHO? The quest for the optimal PET tracer for glioma imaging continues. Nat Clin Pract Neurol 2008;4:470–1.
16. Drzezga A, Souvatzoglou M, Eiber M, Beer AJ, Furst S, Martinez-Moller A, et al. First clinical experience with integrated whole-body PET/MR: comparison to PET/CT in patients with oncologic diagnoses. J Nucl Med 2012;53:845–55.
17. Sauter AW, Wehrl HF, Kolb A, Judenhofer MS, Pichler BJ. Combined PET/MRI: one step further in multimodality imaging. Trends Mol Med 2010;16:508–15.
18. Friese MA, Platten M, Lutz SZ, Naumann U, Aulwurm S, Bischof F, et al. MICA/NKG2D-mediated immunogene therapy of experimental gliomas. Cancer Res 2003;63:8996–9006.
19. Provencher SW. Estimation of metabolite concentrations from localized *in vivo* proton NMR spectra. Magn Reson Med 1993;30:672–9.
20. Beckstead JH. A simple technique for preservation of fixation-sensitive antigens in paraffin-embedded tissues. J Histochem Cytochem 1994;42:1127–34.
21. Kato T, Shinoda J, Nakayama N, Miwa K, Okumura A, Yano H, et al. Metabolic assessment of gliomas using 11C-methionine, [18F] fluorodeoxyglucose, and 11C-choline positron-emission tomography. AJNR Am J Neuroradiol 2008;29:1176–82.
22. Kinoshita Y, Yokota A. Absolute concentrations of metabolites in human brain tumors using *in vitro* proton magnetic resonance spectroscopy. NMR Biomed 1997;10:2–12.
23. Usenius JP, Vainio P, Hernesniemi J, Kauppinen RA. Choline-containing compounds in human astrocytomas studied by 1H NMR spectroscopy *in vivo* and *in vitro*. J Neurochem 1994;63:1538–43.
24. Frahm J, Bruhn H, Gyngell ML, Merboldt KD, Hanicke W, Sauter R. Localized proton NMR spectroscopy in different regions of the human brain *in vivo*. Relaxation times and concentrations of cerebral metabolites. Magn Reson Med 1989;11:47–63.
25. Cohen BM, Renshaw PF, Stoll AL, Wurtman RJ, Yurgelun-Todd D, Babb SM. Decreased brain choline uptake in older adults. An *in vivo* proton magnetic resonance spectroscopy study. JAMA 1995;274:902–7.
26. Toft PB, Leth H, Lou HC, Pryds O, Henriksen O. Metabolite concentrations in the developing brain estimated with proton MR spectroscopy. J Magn Reson Imaging 1994;4:674–80.
27. Lee SG, Kim K, Kegelman TP, Dash R, Das SK, Choi JK, et al. Oncogene AEG-1 promotes glioma-induced neurodegeneration by increasing glutamate excitotoxicity. Cancer Res 2011;71:6514–23.
28. Behrens PF, Ostertag CB, Warnke PC. Regional cerebral blood flow in peritumoral brain edema during dexamethasone treatment: a xenon-enhanced computed tomographic study. Neurosurgery 1998;43:235–40.

29. Kuhmonen J, Sivenius J, Riekkinen PJ Sr, Kauppinen RA. Decrease in brain choline-containing compounds following a short period of global ischemia in gerbils as detected by 1H NMR spectroscopy *in vivo*. NMR Biomed 1994;7: 231–6.

30. Rommel D, Bol A, Abarca-Quinones J, Peeters F, Robert A, Labar D, et al. Rodent rhabdomyosarcoma: comparison between total choline concentration at H-MRS and [18F]-fluoromethylcholine uptake at PET using accurate methods for collecting data. Mol Imaging Biol 2010;12:415–23.

31. Shimizu H, Kumabe T, Shirane R, Yoshimoto T. Correlation between choline level measured by proton MR spectroscopy and Ki-67 labeling index in gliomas. AJNR Am J Neuroradiol 2000;21:659–65.

32. Rand SD, Prost R, Haughton V, Mark L, Strainer J, Johansen J, et al. Accuracy of single-voxel proton MR spectroscopy in distinguishing neoplastic from nonneoplastic brain lesions. AJNR Am J Neuroradiol 1997;18:1695–704.

33. Srinivasan R, Phillips JJ, Vandenberg SR, Polley MY, Bourne G, Au A, et al. *Ex vivo* MR spectroscopic measure differentiates tumor from treatment effects in GBM. Neuro Oncol 2010;12:1152–61.

Supplementary data:

Supplementary Material and Methods

Animal preparation

The animals were housed in standard cages with *ad libitum* access to both food and water. During the imaging sessions, the animals were anesthetized with 1.5% isoflurane vaporized in medical oxygen (1.0 L/min) using a dedicated animal anesthesia unit (Vetland, Louisville, KY, USA). An *i.v.* catheter was placed into the tail vein for the injection of PET tracer and MR contrast agent. The body temperature of the mice was maintained at 37°C during the PET and MR examinations.

Imaging

In addition, T2-weighted (turbo spin echo 3D, TR=3500 ms, TE=188 ms, matrix size: 256x256x104, voxel size: 0.23x0.23x0.22 mm^3, 1 average, acquisition time: 4 min 35 s) and T1-weighted (flash 3D, TR=16 ms, TE=4.6 ms, matrix size: 192x192x72, voxel size: 0.125x0.125x0.110 mm^3, a=25°, 2 averages, acquisition time: 4 min 53 s) sequences were recorded. T1-weighted post-gadolinium sequences were acquired in 17 animals (d8: n=3, d12: n=3, d14: n=6, d16: n=3 and d18: n=2) with an injection of 6.25 µmol Gadopentetic acid contrast agent (Magnevist, BayerSchering Pharma, Berlin, Germany) diluted with saline solution at an injected volume of 62.5 µL. After the measurements, the animals were sacrificed for histology.

Voxel-wise correlation analysis of PET and CSI data

Tumor ROIs were defined in five typical examples (post-implantation days 12-14). In each animal brain 3 different tumor ROIs were created, based on normalized PET, CSI and T2 weighted anatomical MR images. The PET normalization was related to the injected dose in the individual animal and CSI normalization to the tumor-to-brain-

ratios. Voxel-wise PET and CSI data of each ROI was recorded using Inveon research workplace (IRW, Version 3.0, Siemens Healthcare, Knoxville, USA). Pearson correlation coefficients of PET and CSI voxels were calculated using dedicated MATLAB programs, written in house (MATLAB release 2012b, The MathWorks, Inc., USA). Furthermore, tumor volumes based on anatomical T2-weighted MR, PET uptake and CSI data were recorded. Intersections between these volumes were computed. A Venn diagram showing the intersections of the volumes linked to MR anatomy, PET uptake and CSI was compiled using R project (R version 2.15.1 venneuler library, open source).

mRNA expression

On post-implantation days 11 and 15, the tumor, brain and cerebellum from three animals were biopsied using a 4 mm diameter punch (Biopsy punch, #48401, PFM Medical AG, Cologne, Germany), which was guided by MR images. The samples were subsequently homogenized in lysis buffer according to the manufacturer's recommendations (High Pure RNA Tissue Kit, Roche, Basel, Switzerland) using a disperser (T 25 basic, ULTRA-TURRAX, IKA-Werke, Staufen, Germany). RNA samples were stored at -80 °C. Total RNA was isolated from frozen tumor, brain and cerebellum samples and quantified using a photometer (Nanodrop 1000, NanoDrop Technologies, Wilmington, DE, USA). Next, two microgram RNA was used for reverse transcriptase analysis. Real-time PCR was performed using gene-specific oligonucleotide primers for mouse genes. The resulting cDNA was synthesized using Moloney Murine Leukemia Virus (M-MLV) reverse transcriptase (Superscript II, Invitrogen, Carlsbad, CA, USA). The mRNA expression levels of the following transporters and enzymes in the tumor, brain and cerebellum were analyzed: CHT1 (high affinity choline transporter 1, SC5A7 solute carrier family 5 (choline transporter)

member 7, sense: 5'-CAT GAA ATG GTT GCT GGA TG-3', antisense: 5'-TGA ACG CAT GCT GAT AAA GC-3'), CTL1 (choline transporter-like protein 1, sense: 5'-CGG TAC TGT GGC AAA AGG AT-3', antisense: 5'-TGC ATG CTT CAG TTT TCT GG-3'), CTL2 (choline transporter-like protein 2, sense: 5'-CGG ACA AAC CGT TCT TGT TT-3', antisense: 5'-GGT GAT AAC CGC TGG ACA CT-3'), CTL3 (choline transporter-like protein 3, sense: 5'-TCC TTT TCC TGT GCT TTG CT-3', antisense: 5'-TCT GTC CCC TCT TCA TTT GG-3'), CTL4 (choline transporter-like protein 4, sense: 5'-AAG TGC GTC TTC AAG GGC TA-3', antisense: 5'-GTC TCG AGG CTT GTG AAA GG-3'), OCT1 (organic cation transporter 1, SLC22A1 (solute carrier family 22 member 1), sense: 5'-GTA AGC TCT GCC TCC TGG TG-3', antisense: 5'-GCT GTC GTT CTC CTG TAG CC-3'), OCT2 (organic cation transporter 2, SLC22A2 (solute carrier family 22 member 2), sense: 5'-AAA TGG TCT GCC TGG TCA AC-3', antisense: 5'-AGG CCA ACC ACA GCA AAT AC-3'), CKα (choline kinase α, sense: 5'-GCT GTC GTG TGG ATG CTA GA-3', antisense: 5'-GGC ACT GCT GTT GAG TTT GA-3'), CKβ (choline kinase β, sense: 5'-CCA CGG ACT ACC CCA CTA GA-3', antisense: 5'-GAC CAC AGA CCC CAG AAA AA-3'), PHLD (phospholipase D, glycosylphosphatidylinositol specific phospholipase D1, sense: 5'-TCT TGG CAA CAG ATG CAG AC-3', antisense: 5'-CCA GTC AGC TTC CTC CAA AG-3') and aldolase A was used as a housekeeping gene (sense: 5'-TGG GCC TTG ACT TTC TCC TAT-3', antisense: 5'-TGT TGA TGG AGC AGC CTT AGT-3').

Secondary ion mass spectrometry - mass spectrometry imaging (SIMS-MSI)

Mouse brains (control and tumor at post-implantation day 15) were snap-frozen in liquid nitrogen and stored at -80ºC until analysis. The 12 µm thick horizontal brain sections were cut at -20°C using a cryo-microtome (HM525, MICROM, Germany). Tissue sections for SIMS-imaging analysis were mounted on 25 mm x 50 mm x

1.1 mm, Indium Tin Oxide (ITO) coated slides (Delta Technologies, USA) and for additional H&E staining on 76 mm x 26 mm microscope slides (Thermo scientific, MENZEL-GLÄSER, Germany).

Prior to SIMS-MSI analysis slides with mounted tissue sections were placed inside a vacuum desiccator for 30 min, followed by gold-coating using a SC7640 sputter coater (Quorum Technologies New Haven, UK) equipped with a FT7607 quartz crystal microbalance stage and a FT690 film thickness monitor to deposit a 1 nm gold layer. Data was acquired using a Physical Electronics TRIFT II TOF-SIMS (Physical Electronics, USA) equipped with a gold liquid metal ion gun tuned for 22 keV Au^+ primary ions. Images were acquired at a raster size of 162.5 µm over a 10,4 mm x 10,4 mm area (tumor-bearing brain) and at a raster size of 178 µm over a 11,4 mm x 11,4 mm area (control brain) which means that 64 x 64 tiles were measured in both measurement. Each tile was measured for 9 seconds which results in a total measurement time of ten hours per sample. Data was analyzed and visualized using WinCadence software version 4.7.1 (Physical Electronics, USA). Subsequently, H&E staining of the adjacent tissue sections was performed.

Supplementary Results

Animal weight

The average animal weight in grams (mean ± SD) during the various days of the experiment are as follows:

d5: 20.19 ± 1.30, d6: 19.28 ± 1.92, d7: 18.44 ± 1.60, d8: 21.77 ± 2.92, d11: 24.98 ± 2.45, d12: 21.73 ± 4.02, d14: 19.51 ± 2.00, d16: 17.52 ± 4.02 and d18: 18.00 ± 0.00.

^{11}C-choline PET

Tumor choline uptake (%ID/mL) is presented (mean ± SD) as follows: d5: 1.41 ± 0.10, d6: 2.10 ± 0.24, d7: 2.12 ± 0.56, d8: 1.78 ± 0.26, d11: 1.39 ± 0.18, d12: 1.27 ± 0.55, d14: 2.34 ± 0.53, d16: 3.11 ± 1.29 and d18: 3.93 ± 0.28. The corresponding SUV values are as follows: d5: 0.31 ± 0.04, d6: 0.35 ± 0.15, d7: 0.27 ± 0.08, d8: 0.36 ± 0.10, d11: 0.35 ± 0.03, d12: 0.35 ± 0.11, d14: 0.47 ± 0.11, d16: 0.52 ± 0.17 and d18: 0.71 ± 0.05. The values of the tumor-to-brain ratios (Figure 1C) are as follows: d5: 1.12 ± 0.15, d6: 0.97 ± 0.16, d7: 1.12 ± 0.17, d8: 1.23 ± 0.11, d11: 1.23 ± 0.22, d12: 1.25 ± 0.18, d14: 1.45 ± 0.26, d16: 1.07 ± 0.24 and d18: 2.22 ± 0.11. The choline uptake values (averaged over the entire period) in the brain were 1.64 ± 0.84 %ID/mL, 1.87 ± 0.81 %ID/mL in the cerebellum and 1.69 ± 1.28 %ID/mL in the skeletal muscle. The tumor-to-brain ratios ranged from 1.12 ± 0.15 at day 5 to 2.22 ± 0.11 at day 18, while the tumor-to-cerebellum ratios increased between day 5 (0.89 ± 0.08) and day 18 (1.65 ± 0.01) (Figure 1D). The tumor-to-muscle ratios ranged from 1.07 ± 0.12 at day 5 to 2.22 ± 0.11 at day 18.

PET / CSI	^{11}C-choline tumor %ID/mL	^{11}C-choline tumor / brain	^{11}C-choline tumor / cerebellum	^{11}C-choline tumor / muscle
tumor tCho	r = -0.583 P = 0.099	r = -0.680 P = 0.044	r = -0.812 P = 0.008	r = -0.547 P = 0.128
tumor tCho/NAA	r = 0.315 P = 0.409	r = 0.049 P = 0.900	r = 0.071 P = 0.855	r = 0.380 P = 0.313
tumor tCho/ brain tCho	r = 0.839 P = 0.005	r = 0.693 P = 0.038	r = 0.659 P = 0.054	r = 0.456 P = 0.217
tumor tCho/ tCho cerebellum	r = -0.012 P = 0.975	r = 0.106 P = 0.787	r = 0.210 P = 0.587	r = -0.360 P = 0.341

Table 1S: Correlations between the tumor data derived from PET and CSI measurements referenced to different regions and metabolites.

Tumor contrast enhancement

For the estimation of tumor vasculature and the disruption of the blood brain barrier, tumor-to-brain ratios based on the T1-weighed post-gadolinium sequences were calculated. The ratios increase from day 8 until day 16 and then decrease on day 18 as follows: d8: 1.49 ± 0.08, d12: 1.74 ± 0.08, d14: 1.87 ± 0.47, d16: 1.98 ± 0.04 and d18: 1.54 ± 0.67.

mRNA expression

All values were referenced to aldolase A as a housekeeping gene and the reference tissues (brain (b) and cerebellum (c)). In general, higher expression levels were observed in the cerebellum compared with the brain. The expression levels of CHT1 in the tumor on day 11 were equivalent to the expression levels of the normal brain (-

0.77%) but decreased on day 15 (-88.53%). Compared with the cerebellum, the CHT1 expression levels in the tumor were much lower for both days (d11: -267.67%, d15: -587.85%). CTL1 in the tumor displayed high expression levels on day 11 and a small decrease on day 15 compared with the brain tissue (d11: 86.70%, d15: 82.60%) and the cerebellum (d11: 73.43%, d15: 65.24%). The same expression patterns were observed for CTL2 and CTL3 in the tumor (CTL2 (% (b)): d11: 84.43%, d15: 78.26%; CTL2 (% (c)): d11: 63.06%, d15: 48.44%; CTL3 (% (b)): d11: 93.01%, d15: 88.54%; CTL2 (% (c)): d11: 63.62%, d15: 40.35%). CTL4 expression levels in the tumor increased from day 11 to day 15 when referenced to the brain (d11: 35.45%, d15: 64.94%) and the cerebellum (d11: 82.03%, d15: 90.24%). The OCT1 and OCT2 expression levels in the tumor increased from day 11 to day 15 compared with the expression level in the brain (OCT1: d11: 33.26%, d15: 68.13%; OCT2: d11: 4.27%, d15: 12.83%) but displayed reduced expression levels compared with the cerebellum (OCT1: d11: -313.05%, d15: -97.24%; OCT2: d11: -29.99%, d15: -18.37%). The expression levels of both CKα and CKβ in the tumor were slightly increased at day 11 compared with day 15 with brain tissue as the reference (CKα: d11: 51.48%, d15: 50.14%; CKβ: d11: 84.80%, d15: 82.09%). The same was observed for the CKβ expression levels in the tumor referenced to the cerebellum expression data (CKβ: d11: 71.88%, d15: 66.86%). However, lower expression levels of CKα in the tumor were observed on day 11 compared with the cerebellum (d11: -2.95%, d15: -5.78%). For the PHLD results, the expression levels in the tumor decreased from 84.00% to 12.04% compared with the brain and from 51.99% to -163.89% compared with the cerebellum. Most of the transporters and enzymes displayed higher expression levels in the cerebellum compared with the brain cortex (range: 26.36% [OCT2] – 83.84% [OCT1]). One exception was CTL4, which

displayed lower expression level (-259.11%) in the cerebellum compared with the brain cortex.

Supplementary Discussion

Glunde et al. have suggested that different types of cancer use different choline transport mechanisms depending on the tissue of origin (1). For example, in breast cancer, Eliyahu et al. have observed the upregulation of OCT2, CHT1 and CKα (2). Interestingly, CHT1 seems to be downregulated in the tumor compared with normal brain and cerebellum in our tumor model, while the other transporters were upregulated. CKβ displayed higher expression levels compared with CKα. These transport systems and enzymes contribute to the increase in choline uptake. Kent et al. have shown that elevated choline kinase activity in highly malignant astrocytomas may cause an increase in PC levels (3). In addition to being transported from the circulation, free choline is synthesized from different pathways. In particular, phospholipase D catalyzes the synthesis of free choline directly from PC (4), which is also overexpressed. Interestingly, this corresponds to a decrease in tCho levels. Most of the transporters were downregulated from day 11 to day 15, which may suggest the progressive de-differentiation of the tumor. Regarding the potential role of the cerebellum as a reference tissue, all transporter and enzymes except for CTL4 exhibited higher expression levels compared with the brain. This might also explain the increased tCho levels and enhanced choline uptake in the cerebellum compared with the normal brain tissue. Therefore, we suggest that the cerebellum would be an inferior reference tissue.

Regarding the tCho levels and the %ID/mL in the normal contralateral brain and cerebellum as potential reference tissues, we observed higher levels of accumulation in the cerebellum (tCho: 2.86 ± 2.54 $x10^4$ a.u., %ID/mL: 1.87 ± 0.81) compared with the brain (tCho: 2.72 ± 1.33 $x10^4$ a.u., %ID/mL: 1.64 ± 0.84). This result is also reflected by the PCR data that shows higher expression levels of both the transporters and enzymes in the cerebellum compared with the normal brain tissue.

These high expressions lead to increased ^{11}C-choline uptake in the cerebellum and reduced tumor-to-cerebellum and tumor-to-brain ratios. Histological data has shown that the distribution of the high affinity transporters throughout the brain is not homogenous, the cerebellum displays low cholinergic innervation (5) and choline is accumulated only by low affinity systems (6). Based on our results, these observations suggest that the lower affinity transport systems primarily contribute to increased choline accumulation. Traiffort et al. and Machova et al. have shown that CTL1 is involved in this process (7, 8). It is known that malignant gliomas have the ability to spread along CNS white matter fiber tracts, which is often neglected by morphological imaging (9). The decrease in NAA values observed in this study, which ranged from 137.00 x10^4 a.u (d5) to 1.62 x10^4 a.u (d18) can indicate a tumor spread and therefore support this hypothesis. The tCho levels observed in the cerebellum displayed a large variability that is most likely due to shimming challenges and field inhomogenities. In this report, the air tissue interfaces, which involve the ear canals, the complexity of the middle and the inner ear structures, make a field homogenization difficult to produce, especially when taking the small spatial structures of the mouse brain into account. This is also reflected by the high level of shim strengths required for the mouse cerebellum (10).

Supplementary References

1. Glunde K, Bhujwalla ZM, Ronen SM. Choline metabolism in malignant transformation. Nat Rev Cancer.11:835-48.

2. Eliyahu G, Kreizman T, Degani H. Phosphocholine as a biomarker of breast cancer: molecular and biochemical studies. Int J Cancer. 2007;120:1721-30.

3. Kent C. Regulation of phosphatidylcholine biosynthesis. Prog Lipid Res. 1990;29:87-105.

4. Boulanger Y, Labelle M, Khiat A. Role of phospholipase A(2) on the variations of the choline signal intensity observed by 1H magnetic resonance spectroscopy in brain diseases. Brain Res Brain Res Rev. 2000;33:380-9.

5. Misawa H, Nakata K, Matsuura J, Nagao M, Okuda T, Haga T. Distribution of the high-affinity choline transporter in the central nervous system of the rat. Neuroscience. 2001;105:87-98.

6. Yamamura HI, Snyder SH. High affinity transport of choline into synaptosomes of rat brain. J Neurochem. 1973;21:1355-74.

7. Machova E, O'Regan S, Newcombe J, Meunier FM, Prentice J, Dove R, et al. Detection of choline transporter-like 1 protein CTL1 in neuroblastoma x glioma cells and in the CNS, and its role in choline uptake. Journal of neurochemistry. 2009;110:1297-309.

8. Traiffort E, Ruat M, O'Regan S, Meunier FM. Molecular characterization of the family of choline transporter-like proteins and their splice variants. Journal of neurochemistry. 2005;92:1116-25.

9. Amberger VR, Hensel T, Ogata N, Schwab ME. Spreading and migration of human glioma and rat C6 cells on central nervous system myelin in vitro is correlated with tumor malignancy and involves a metalloproteolytic activity. Cancer research. 1998;58:149-58.

10. Frahm J, Bruhn H, Gyngell ML, Merboldt KD, Hanicke W, Sauter R. Localized proton NMR spectroscopy in different regions of the human brain in vivo. Relaxation times and concentrations of cerebral metabolites. Magn Reson Med. 1989;11:47-63.